Journal of Power Sources 182 (2008) 240–253

Contents lists available at ScienceDirect

Journal of Power Sources

journal homepage: www.elsevier.com/locate/jpowsour

Dynamic first principles model of a complete reversible fuel cell system

Tim M. Brown [a], Jacob Brouwer [a,*], G. Scott Samuelsen [a], Franklin H. Holcomb [b], Joel King [c]

[a] National Fuel Cell Research Center (NFCRC), University of California, Irvine, Irvine, CA 92697-3550, United States
[b] U.S. Army Engineer Research & Development Center, Construction Engineering Research Lab, 2902 Newmark Drive, Champaign, IL 61826-9005, United States
[c] Alion Science and Technology, U.S. Army National Automotive Center, AMSRD-TAR/N (MS 289), Warren, MI 48397-5000, United States

ARTICLE INFO

Article history:
Received 4 February 2008
Received in revised form 7 March 2008
Accepted 16 March 2008
Available online 4 April 2008

Keywords:
Reversible fuel cell
Dynamic model
PEM fuel cell
PEM electrolyzer
Hydride tank

ABSTRACT

A dynamic model of a discrete reversible fuel cell (RFC) system has been developed in a Matlab Simulink® environment. The model incorporates first principles dynamic component models of a proton exchange membrane (PEM) fuel cell, a PEM electrolyzer, a metal hydride hydrogen storage tank, and a cooling system radiator, as well as empirical models of balance of plant components. Dynamic simulations show unique charging and discharging control issues and highlight factors contributing to overall system efficiency.

1. Background and introduction

Reversible fuel cell (RFC) systems act as "rechargeable" energy storage devices designed to work as turn-key systems with electricity being the only input and output. This may allow future systems to replace traditional chemical storage batteries in applications where the potential performance benefits outweigh the cost tradeoffs [1]. The major components in an RFC system are a fuel cell, an electrolyzer (*unitized* RFC systems use just one device to perform both functions, *discrete* systems have separate fuel cell and electrolyzer devices), and a hydrogen storage tank. Numerous balance of plant components are also necessary for a practical system [2]. It is only through thorough modeling of all these components that true system efficiencies can be estimated. Fig. 1 shows a schematic diagram of the RFC system modeled in this work, demonstrating the complex auxiliary components and circuitous integration of all of the parts.

The RFC system is "charged" by supplying electricity to an electrolyzer that disassociates water yielding hydrogen and oxygen. The oxygen is vented to the atmosphere and the hydrogen is stored in the hydrogen tank. The current system uses a reversible metal hydride compound confined in an aluminum tank for hydrogen storage. When power is needed from the system, hydrogen is supplied by the tank to the fuel cell where it is combined with air to produce electricity, heat, and water.

The RFC energy storage system is unique when compared to traditional chemical batteries because the power capability, energy storage capacity, and recharge rate are all determined independently [3]. With the exception of shared controls and plumbing, the hydrogen tank capacity solely determines the energy storage of the system, the fuel cell power output governs the power output of the system, and the electrolyzer power determines the "recharge" rate of the system. These properties lead to system advantages in specialized applications, particularly for those applications that require low to moderate power, long duration performance, and/or strict weight requirements. The fuel cell and electrolyzer can be sized as needed for the power requirement, while the hydrogen storage tank can simply be sized up or down, independently, to meet the energy storage requirement. A traditional chemical battery would require increases in all parameters in order to meet the demands of just one of these design criteria. Consequently, a fuel cell/electrolyzer system can theoretically achieve a better energy density than even state-of-the-art chemical batteries [4].

In order to evaluate the performance of a fuel cell rechargeable energy system, to garner insight into the dynamic response characteristics of the system and individual components, and to design superior systems in the future, a dynamic model of a RFC system is developed in a modular Matlab Simulink® framework.

1.1. Experimental RFC system description

The particular regenerative fuel cell system being modeled was designed to replace lead-acid batteries onboard a U.S. Army Stryker vehicle and consists of a 5.5 kW fuel cell, a 3.6 kW electrolyzer, and

* Corresponding author. Tel.: +1 949 824 1999; fax: +1 949 824 7423.
E-mail address: jb@nfcrc.uci.edu (J. Brouwer).

0378-7753/$ – see front matter © 2008 Elsevier B.V. All rights reserved.
doi:10.1016/j.jpowsour.2008.03.077

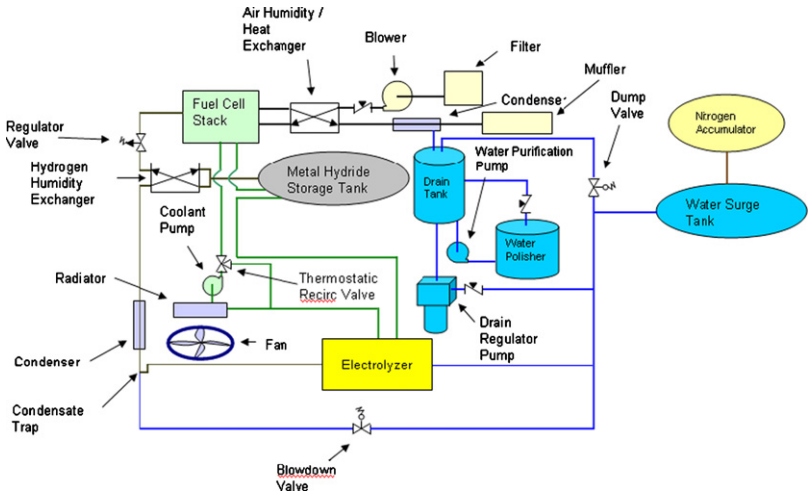

Fig. 1. Schematic representation of the experimental RFC system.

a hydride tank capable of holding 10,000 standard liters of hydrogen. This combination of components is assembled using parts that are commercially available, with little effort made to optimize the system for any particular performance goal. As a result, the performance reported herein should not be construed as optimal. Future system performance improvements are very likely through better component sizing, integration, and optimization, which is outside the scope of this paper.

The Stryker vehicle is equipped with a large array of advanced electronic surveillance equipment, which can be utilized in a "silent-watch" mode whereby the electronics are powered for an extended time without running the diesel prime mover. The system is charged by excess power from the vehicle's alternator during normal operation, but when silent operation is desired, the main vehicle combustion engine is turned off, the vehicle becomes stationary, and the batteries power the onboard electronics. The proposed RFC system would seamlessly replace the lead-acid battery pack while ideally providing longer silent-watch duration due to the efficiency and energy storage capabilities of the RFC system.

RFCs are well suited to military applications because of the desire to use common fuels. Jet Propulsion 8, or JP-8, is a kerosene-based fuel that is the single battlefield fuel for Department of the Army applications including electric power generators, wheeled and tracked vehicles, aircraft, stoves, and heaters. An immense logistical effort is necessary to move the enormous quantities of JP-8 fuel required for military operations into a forward deployed overseas location. Delivered costs of JP-8 to Army combat platforms have been estimated to be at least \$30–\$40 gallon^{-1} for overland transport, and greater than \$400 gallon^{-1} for air delivery [5].

Because of the "single battlefield fuel" mandate, fuel cell generators or other clean and efficient hydrogen consuming devices cannot be utilized on the battlefield unless the hydrogen is obtained from reformation of JP-8 or by other means with existing battlefield resources. Consequently, an RFC system having electricity as the only input and output is one potential fuel cell technology available to the military. This type of RFC device could be recharged by alternators attached to diesel engines in exactly the same manner batteries are used today. This could benefit military applications that currently rely on lead-acid batteries for electrical storage, without violating the single fuel forward mandate.

A proton exchange membrane (PEM) fuel cell and electrolyzer were chosen for this application because of their relatively high power density, inherent load following capability, and relative technological maturity compared to other fuel cell and electrolyzer technologies. The fuel cell is fueled by pure hydrogen produced from electrolysis of deionized water and stored in a metal hydride tank. Metal hydride absorbs and desorbs hydrogen in exothermic and endothermic reactions, respectively [6]. Consequently, the RFC system utilizes an integrated, dual-purpose, cooling loop that provides coolant to the hydride tank during the exothermic charging process, and fluid warmed by the fuel cell waste heat to the tank during the endothermic hydrogen release process. The use of a metal hydride tank therefore creates a synergy that enables fuel cell waste heat to provide energy for hydrogen storage, eliminating the need for compression energy that would be required if compressed gas storage was used.

1.2. RFC models in the literature

Several RFC system models and analyses have been reported in the literature. Bolwin calculated static RFC system energy and power densities based on a list of component masses, efficiencies, and power densities [3]. Ulleberg developed a semi-empirical, bulk, alkaline electrolyzer model for use in hydrogen energy system simulations and showed an example system integration including renewable energy sources and compressed gas hydrogen storage [7]. Barbir et al. statically compared the efficiencies of unitized and discrete PEM RFCs using generalized polarization curves and parasitic losses proportional to system power [4]. Busquet et al. used an empirical model to well predict fuel cell and electrolyzer performance, but did not include parasitic ancillary loses or energy storage [8]. Khan and Iqbal created a dynamic Simulink model of a wind powered fuel cell electrolyzer system, but did not model parasitic loads or heat transfer within the devices [9]. Görgün produced a detailed dynamic PEM electrolyzer model for future use in fuel cell electrolyzer systems that includes pressurized hydrogen storage and membrane water transport. However, the model does not include heat transfer or GDL gas diffusion effects [10]. Maclay et al. developed a comprehensive empirical dynamic residential RFC model used to analyze RFC applications to renewable energy storage, though the analysis does not include efficiency losses due to ancillary components or hydrogen storage effects [11]. The model reported herein differs from others in the literature due to the exhaustive, first principles approach that has been undertaken. This approach enables simulation of the dynamic responses of all the major system components and all of the interactions amongst the components and in the balance of plant, along with comprehensive energy and efficiency analyses that include all significant ancil-

lary components of a complete RFC system. The model is detailed enough to accurately simulate this type of system, yet simple enough to use in control system development and analysis studies.

2. Model description

The RFC model simulates the experimental RFC system described above as closely as possible by requiring only the same inputs as provided to the experimental system. Operating input parameters include ambient air temperature and humidity, desired operating mode (power mode or charge mode) and desired fuel cell current when in power mode. Extensive material property data, component geometry, and dimensional information are also entered into the model to simulate the properties of the experimental system components.

The model assumes that maximum power is always available to the electrolyzer when it is operating in charge mode. This simplifying assumption allows the dynamics of the system to be analyzed separately from the electrical power source (an alternator attached to a diesel engine in the current experiment). This assumption would not be valid in all circumstances; for example, if the electrolyzer was powered by an intermittent source such as a photovoltaic panel, the maximum power would not always be available. Such a case would yield interesting results, but may give little information about the performance of the RFC system itself, which is of primary interest in the current effort.

Despite the attempt to make this model as comprehensive as possible, numerous balance of plant components that are necessary for a real system to work have been assumed to have no impact on the dynamic performance of the system. These balance of plant components that are assumed to have instantaneous response characteristics mainly include plumbing items such as valves, piping, and filters. For example, the deionized water system necessary for robust electrolysis has been neglected and flow pressure losses have not been accounted for in any part of the model. In addition, no effort has been made to produce a physical model of the enthalpy and humidity exchange between fuel cell cathode outlet and the fuel cell inlet. While these omissions affect system performance the major contributors to overall system performance are captured. The effects of these missing balance of plant parts could be introduced into the model in a later study, but are assumed to be minimal in the current analyses.

Each of the main components of the RFC model (fuel cell, electrolyzer, metal hydride tank, radiator) is simulated using a dynamic, first principles approach. The environments within any control volume of the models are assumed to comprise ideal, "perfectly stirred" conditions for fluids and homogenous compositions for solids. The following sections will describe the conservation equations and physics modeled for each of the four main components. The equations and approach used for each of the models are similar, but the actual terms and physical properties, and processes simulated, vary with each component model. Table 1 shows the number of control volumes and the particular physics modeled for each component.

Table 1
Control volumes and physical relations modeled for each of the four major system components

Model attribute	Fuel cell	Electrolyzer	Hydride tank	Radiator
Number of control volumes	8	6	31	8
Conservation of energy	X	X	X	X
Conservation of mass	X	X	X	X
Heat conduction	X	X	X	X
Heat convection	X	X	X	X
Diffusion	X	X		
Chemical reactions			X	
Electrochemical reactions	X	X		

2.1. Metal hydride tank model

The metal hydride tank is modeled as a cylinder comprised of 30 nested cylindrical shells as shown in Fig. 2. The hydrogen gas can enter or exit from only one end of the tank. In addition to the reactive material "shells" pictured in Fig. 2, a thin aluminum outer enclosure is also modeled that does not participate in the hydriding reaction, but simulates the canister that holds the powdered material in an actual tank. Note that heat transfer physics are affected by the thermal mass, conduction, and convection heat transfer properties of the aluminum tank. Previous work [12] has shown that accurate tank temperature and hydrogen absorption/desorption results can be obtained from a metal hydride model without accounting for gaseous mass transport within the hydride bed because the timescales of hydrogen diffusion through the porous hydride material are several orders of magnitude faster than the physics associated with heat transfer within the tank. As a result, hydrogen absorption and desorption are rate-controlled by heat transfer physics [12]. Likewise, it has been shown that gaseous heat transfer and gaseous energy conservation can also be neglected as the quantity of energy transferred to or from the gas is several orders of magnitude smaller than the energy of the hydriding reaction, on a per mass basis [12]. These simplifications enable the relatively large number of 30 nodes to be modeled without creating an overwhelming computational burden. A minimum of 30 nodes was found to be necessary to accurately predict the heat

Fig. 2. Drawing showing nodal discretization used in the metal hydride tank model.

transfer, and consequently the hydrogen absorption level, in the tank due to the heavy dependence of absorption on temperature and the relatively poor heat transfer characteristics of powdered metal hydride.

No absorption–desorption hysteresis is accounted for in the present model. The hysteresis associated with the $LaNi_5$ alloy used herein is 0.13, meaning that 13.8% more pressure is required to fill the tank than is returned when it is emptied [6]. This effect would serve to lower the overall RFC system efficiency.

2.1.1. Rate of hydride reaction

The hydriding reaction rate is modeled as

$$\dot{m}_{\text{reaction}} = -C_a \, e^{(-E_a/RT)} \ln\left(\frac{P_g}{P_{vH}}\right)(\rho_{\text{full}} - \rho_{\text{node}})V_S \quad (1)$$

where C_a is the reaction rate constant, E_a is the activation energy, R is the ideal gas constant, and ρ_{full} and ρ_{node} are the saturated and nodal densities of the solid alloy, respectively [13]. P_g is the hydrogen pressure within the node, and due to the fast transport of hydrogen through the powered metal, P_g is always assumed to be equal to the head pressure at the inlet to the tank. P_{vH} is the pressure predicted by the van't Hoff equation [6]:

$$\ln(P_{vH}) = \frac{\Delta H}{RT_g} - \frac{\Delta S}{R} \quad (2)$$

The values of enthalpy of reaction, ΔH, and the change in entropy for the reaction, ΔS, were experimentally determined for the given hydride alloy being used [6].

2.1.2. Solid alloy conservation of mass

The volume of solid hydride alloy within a node, V_S, is equal to the non-porous volume of the node:

$$V_S = (1 - \varepsilon)V_{\text{node}} \quad (3)$$

where ε is the porosity of the metal hydride. The mass of the solid, m_S, in the node is

$$m_S = \rho_{\text{node}} V_S \quad (4)$$

The mass in a node can only change by absorbing or desorbing hydrogen. The mass conservation equation is consequently written as

$$\frac{\partial m_S}{\partial t} = \dot{m}_{\text{reaction}} \quad (5)$$

This can be integrated to find the instantaneous nodal mass. When plugged back into Eq. (4), this gives the value of metal hydride density needed to calculate the rate of hydrogen absorption given by Eq. (1).

2.1.3. Conservation of energy

The change in energy of the solid alloy in each node is due to three processes: (1) conduction with solid in surrounding nodes, (2) heat release or generation during the sorption reaction, and (3) mass change via hydrogen sorption. The energy conservation equation for the solid within each node is therefore:

$$\frac{\partial E_S}{\partial t} = \dot{Q}_{\text{conduction}} + \dot{m}_{\text{reaction}} \Delta H \quad (6)$$

where the rate of change of solid energy can be written as

$$\frac{\partial E_S}{\partial t} = \frac{\partial(\rho_{\text{node}} V_S C_h T_S)}{\partial t} \quad (7)$$

The nodal solid temperature can be found by combining (6) and (7) and numerically integrating.

As mentioned previously, for computational efficiency and negligible error, the temperature of the hydrogen gas in each node is assumed to be the same as the temperature of the solid metal hydride in that node. Consequently, in all parts of the tank:

$$T_g = T_S \quad (8)$$

2.1.4. Heat transfer

Heat transfer within the tank is governed by Fourier's law:

$$\dot{Q}_{\text{conduction}} = -k_s A \frac{\partial T}{\partial x} \quad (9)$$

where A is the cross-sectional area between adjacent nodes and x is the distance between nodal centers. Eq. (9) applies to conduction between the metal hydride nodes and between the outermost node and the aluminum enclosure. Convective heat transfer described by Newton's Law of Cooling takes place between the outer surface of the aluminum enclosure and the circulating coolant as follows:

$$\dot{Q}_{\text{convection}} = hA_c \, dT \quad (10)$$

Here A_c refers to the outer surface area of the aluminum canister.

2.1.5. Model parameters

The system modeled in this paper uses three individual, cylindrical tanks cooled by submersion in a flowing water bath, which approximates the experimental configuration. The specifications for these tanks are given in Table 2.

Table 2
Metal hydride tank parameters

Parameter	Value	Units	Reference
Number of tanks	3		Per design
Hydride material	$LaNi_5$		Per design
Canister material	Aluminum		Per design
Canister thickness	1.6	mm	Per design
Total hydrogen capacity	10,000	SL	Per design
Maximum pressure, P_{max}	689.5	kPa	Per design
Length, l	0.384	m	Per design
Diameter, d	0.148	m	Per design
Hydride conduction coefficient, k_h	1.0	$W(m\,K)^{-1}$	[14]
Aluminum conduction coefficient, k_{Al}	237	$W(m\,K)^{-1}$	[15]
Hydride specific heat, C_h	418.7	$J(kg\,K)^{-1}$	[16]
Al specific heat, C_{Al}	903	$J(kg\,K)^{-1}$	[15]
Density of Al, ρ_{Al}	2700	$kg\,m^{-3}$	[15]
Density of hydride metal, ρ_h	8300	$kg\,m^{-3}$	[6]
Solid porosity, ε	0.44		Calculated
Activation energy, E_a	31,000	$J\,mol^{-1}$	[14]
Reaction rate constant, C_a	2800	s^{-1}	[17]
Enthalpy of reaction, ΔH	30,800	$J\,mol^{-1}$	[6]
Entropy of reaction, ΔS	108	$J(mol\,K)^{-1}$	[6]
Convection coefficient between canister and coolant, h	700	$W(m^2\,K)^{-1}$	[12][a]

[a] This value was established experimentally for a cylindrical tank subjected to a circulating water bath.

2.2. PEM fuel cell model

The PEM fuel cell model used in this system model was developed by Mueller et al. at UC Irvine and is described completely in a multi-nodal form in [18]. The bulk version of the model used herein is similar, with the primary differences being the number of nodes, the number of cells in the stack, and the dimensions of the different parts of the stack. The current first principles PEM fuel cell model resolves conservation of mass, conservation of energy, and species conservation for each species and layer within a repeat cell unit of the stack.

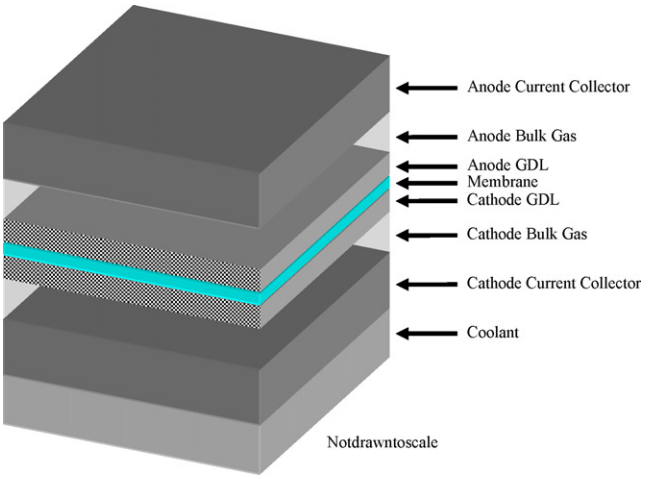

Fig. 3. Diagram showing eight control volumes modeled in the PEM fuel cell component.

The model is divided into eight control volumes: anode and cathode gas diffusion layers, bulk gas chambers, current collectors, membrane, and cathode side coolant channel, as shown in Fig. 3. The first principles approach enables prediction of species concentrations and temperatures for each gas or solid in each layer of the cell repeat unit and the output cell voltage at any time. The stack outputs are simply determined by multiplying or adding the cell repeat unit outputs as determined by the number of series or parallel cells in the stack. For example, for unit cells connected in series the total stack voltage is given by

$$V_{\text{total}} = nV_{\text{cell}} \tag{11}$$

where n is the number of cells in series. In this case the total stack current is the unit cell current. Similar calculations are used to determine total stack species flux values.

The multi-nodal model reported in [18] has been validated against actual operating data from several PEM fuel cells. However, due to the large computational requirements of the complex multi-nodal model, the reduction to just one node has been made to allow integration into the larger RFC system model. Experience shows that this model still produces good predictions of stack temperature, voltage, and outlet species concentrations.

2.2.1. Mass conservation

Mass must be conserved in the bulk gas, GDL, and membrane sections of the fuel cell model while tabulating the proper species concentrations of hydrogen, oxygen, nitrogen, and water. The general species conservation equation for a control volume can be written as

$$\frac{\mathrm{d}n}{\mathrm{d}t} = \dot{n}_{\text{in}} - \dot{n}_{\text{out}} + \dot{n}_{\text{react}} + \sum \dot{n}_{\text{diffuse}} \quad \text{(general form)} \tag{12}$$

where $\dot{n}_{\text{in}}$ and $\dot{n}_{\text{out}}$ are the convective molar fluxes in and out of the control volume, $\dot{n}_{\text{react}}$ is the molar rate of species production, and $\sum \dot{n}_{\text{diffuse}}$ is the sum of the species diffusion rates. This is the most general mass conservation equation. Certain terms drop out depending upon the particular control volume that is being modeled. For example, only the reaction and diffusion terms are used in the GDL layers where gases diffuse and react:

$$\frac{\mathrm{d}n}{\mathrm{d}t} = \dot{n}_{\text{react}} + \sum \dot{n}_{\text{diffuse}} \quad \text{(GDL)} \tag{13}$$

Only diffusion and bulk convective flow terms are used in the bulk gas layers because no reactions are occurring:

$$\frac{\mathrm{d}n}{\mathrm{d}t} = \dot{n}_{\text{in}} - \dot{n}_{\text{out}} + \sum \dot{n}_{\text{diffuse}} \quad \text{(bulk gas layers)} \tag{14}$$

And the membrane species conservation equation contains only diffusion terms with no bulk fluid flow or reaction:

$$\frac{\mathrm{d}n}{\mathrm{d}t} = \sum \dot{n}_{\text{diffuse}} \quad \text{(membrane)} \tag{15}$$

Species conservation is maintained by integrating these equations for each species in each control volume within the model.

For each control volume, relative humidity is calculated as a function of temperature. Any mass of water exceeding saturation is modeled as condensed liquid.

2.2.2. Energy conservation

The general conservation of energy equation used in each fuel cell control volume is written as

$$mC_v \frac{\mathrm{d}T}{\mathrm{d}t} = \sum \dot{m}_{\text{in}} h_{\text{in}} - \sum \dot{m}_{\text{out}} h_{\text{out}} + \sum \dot{Q}_{\text{ht}} + \sum \dot{Q}_{\text{react}} \quad \text{(general form)} \tag{16}$$

where, on the left side, m is the mass of the component, C_v is the constant volume specific heat, T is temperature, and t is time. On the right, $\dot{m}_{\text{in}}$ and $\dot{m}_{\text{out}}$ are the mass transfer rates entering and exiting the control volume and h_{in} and h_{out} are the associated enthalpy values, respectively. Heat transfer with surrounding nodes is given by $\dot{Q}_{\text{ht}}$ and any heat generated or consumed by chemical reactions is given by $\dot{Q}_{\text{react}}$. Again, the terms used depend upon the fuel cell component being analyzed. For the current collectors, Eq. (16) reduces to

$$m_{\text{solid}} C \frac{\mathrm{d}T}{\mathrm{d}t} = \sum \dot{Q}_{\text{ht}} \quad \text{(current collectors)} \tag{17}$$

because the solid components have no enthalpy transferred by convection nor any reactions occurring within the solid. For the MEA (both GDL layers and the membrane are assumed to be at the same temperature) all of the terms in Eq. (16) are used with the caveat that the enthalpy flow term refers to energy transferred via diffusion, not bulk convective flow:

$$\left(\sum m_{\text{gas}} C_v + \sum m_{\text{solid}} C\right) \frac{\mathrm{d}T}{\mathrm{d}t} = \sum \dot{m}_{\text{diffuse}} h_{\text{diffuse}} + \sum \dot{Q}_{\text{ht}} + \sum \dot{Q}_{\text{react}} \quad \text{(MEA)} \tag{18}$$

For the bulk gas layers, energy is transferred by heat, bulk convective flow, and diffusion, but no reaction energy is included:

$$\left(\sum m_{\text{gas}} C_v + \sum m_{\text{solid}} C\right) \frac{\mathrm{d}T}{\mathrm{d}t} = \sum \dot{m}_{\text{in}} h_{\text{in}} - \sum \dot{m}_{\text{out}} h_{\text{out}} + \sum \dot{m}_{\text{diffuse}} h_{\text{diffuse}} + \sum \dot{Q}_{\text{ht}} \quad \text{(bulk gas layers)} \tag{19}$$

Again, the model simultaneously integrates these equations to calculate the temperature of each control volume.

2.2.3. Heat transfer

Heat is transferred between layers in the fuel cell model by conduction and convection, as described in Section 2.1.4 by Eqs. (9) and (10). Heat conduction occurs between each current collector and

the corresponding GDL and heat convection occurs between each bulk gas and the respective current collectors and GDLs. Additionally, convection heat transfer between the coolant and the cathode current collector removes heat from the cell.

Convection coefficients are determined using the Nusselt number, *Nu*:

$$h = \frac{Nu \times k_f}{D_H} \tag{20}$$

where k_f is the fluid conduction heat transfer coefficient and D_H is the hydraulic diameter of the channel being modeled.

2.2.4. Diffusion

Diffusion of gases from the bulk gas flow channels to the GDLs plays an important role in modeling fuel cell behavior because poor gas transport to reaction sites can lead to concentration losses. This model accounts for diffusion of gases from the bulk phase to the GDL by calculating a mass transport coefficient:

$$g_m = \frac{Sh \times D_m}{D_H} \tag{21}$$

where *Sh* is the Sherwood number and D_m is the diffusion coefficient. This is then used to calculate a total resistance, $R_{diffuse}$, to diffusion:

$$R_{diffuse} = \frac{A}{(1/g_m) + (t_{GDL}/D_m^{eff})} \tag{22}$$

where D_m^{eff} is the effective diffusion coefficient modified via the Bruggeman relation:

$$D_m^{eff} = \varepsilon_{GDL}^{3/2} D_m \tag{23}$$

used to account for porosity (ε_{GDL}) and tortuosity in the GDL, and t_{GDL} is the thickness of the catalyst layer. Species flux is calculated as

$$\dot{n}_{diffuse} = R_{diffuse}(C_2 - C_1) \tag{24}$$

where C_2 and C_1 are the molar concentrations in the bulk gas phase and GDL.

2.2.5. Water transport

Water can be transported through the ionic membrane via the process of osmotic drag whereby water molecules are effectively "dragged" from the anode to the cathode by proton transport mechanisms in the membrane. Additionally, water can "back-diffuse" from the cathode to the anode due to a concentration gradient. Both of these processes are accounted for in the current model because membrane water content significantly impacts cell performance (especially membrane protonic conductivity).

The rate of water molecules transported by osmotic drag (θ_{H_2O}) is directly proportional to the number of protons transferred through the membrane:

$$\theta_{H_2O} = \frac{n_d}{AF} \tag{25}$$

where n_d is the membrane water content dependent drag coefficient:

$$n_d = \frac{2.5\lambda}{22} \tag{26}$$

$$\lambda = 0.043 + 17.81a - 39.85a^2 + 36a^3, \quad \text{for } 0 < a \le 1 \tag{27}$$

and *a* is the water activity as given by Springer et al. [19]. Water diffusion due to the concentration gradient between the electrodes is determined by

$$\Psi_{H_2O} = D_w A \frac{C_c - C_a}{t} \tag{28}$$

where D_w is the diffusion coefficient and *t* is the membrane thickness. The diffusion is given as

$$D_w = D_\lambda \exp\left[2416\left(\frac{1}{303} - \frac{1}{T}\right)\right] \tag{29}$$

where

$$D_\lambda = \begin{cases} 10^{-6} & \text{for } \lambda < 2 \\ [1 + 2(\lambda - 2)] \times 10^{-6} & \text{for } 2 \le \lambda \le 3 \\ [3 - 1.67(\lambda - 3)] \times 10^{-6} & \text{for } 3 < \lambda < 4.5 \\ 1.25 \times 10^{-6} & \text{for } 4.5 \le \lambda \end{cases} \tag{30}$$

2.2.6. Electrochemistry

The rates of the electrochemical reactions occurring in the fuel cell are considered instantaneous in the current model because the timescales of these reactions are far faster than those associated with the other physics included in the model [18]. The electrochemical potential of the reactions is modeled using the Nernst equation coupled with equations for ohmic and activation polarization losses as given by Eq. (31), for anode and cathode compartments both operated at the same pressure:

$$V = -\frac{\Delta G(T)}{nF} + \frac{RT}{nF}\ln\left[\frac{X_{H_2}X_{O_2}^{1/2}}{X_{H_2O}}P^{1/2}\right] - a_c\frac{RT}{nF}\ln\left(\frac{i}{i_0}\right) - iR \tag{31}$$

The first term provides the theoretical potential based on Gibb's free energy as a function of temperature. The change in Gibb's energy is given by

$$\Delta G(T) = (-241.9495 + 0.0411 \times T + 1.0641 \times 10^{-5} \times T^2 - 2.4087 \times 10^{-9} \times T^3) \times 1000 \tag{32}$$

The second term in Eq. (31) modifies the theoretical potential to account for the operating pressure, temperature, and species concentrations. The third term is a voltage reduction due to activation losses derived from the Tafel expression, and the final term is a voltage reduction due to Ohm's law, where the resistance, *R*, is a membrane water content dependent term:

$$R = (0.005139\lambda - 0.00326)\exp\left[1268\left(\frac{1}{303} - \frac{1}{273 + T}\right)\right] \tag{33}$$

The rates of all reactions are modeled as instantaneous and proportional to the current:

$$\dot{n}_{react} = \frac{i}{nF} \tag{34}$$

where *i* is the operating current, *F* is Faraday's constant, and *n* is the number of moles of electrons transferred during the reaction per mole of the species reacted. Eq. (34) therefore assumes infinitely fast reaction with perfect electron transfer by every reaction.

Concentration polarization has been neglected in this model because the RFC system never enters the operation regime where concentration losses become significant. The maximum current density of the fuel cell is 490 mA cm^{-2} when operating at full power of 5.5 kW.

2.2.7. Fuel cell model parameters

Several parameters used in this system model are given in Table 3.

2.3. PEM electrolyzer

The electrolyzer model is based closely on the fuel cell model. It too is a bulk model utilizing the same fundamental equations

Table 3
Fuel cell model parameters

Parameter	Value	Units	Reference
Number of cells in series	33	NA	Per design
Exchange current density, i_0	10	$A\,m^{-2}$	[20]
Activation polarization coefficient, a_c	0.5		[20]
Operating pressure, P_o	1.0	atm	Per design
Dimension of cell	0.2258×0.2258	m	Per design
Air utilization, μ_{air}	50	%	Per design
Depth of anode gas channel	0.001	m	Per design
Depth of cathode gas channel	0.001	m	Per design
Depth of cooling channel	0.003	m	Per design
Thickness of GDL, t_{GDL}	0.0002	m	Per design
Thickness of electrolyte	0.00015	m	Per design
Thickness of separator plates	0.002	m	Per design
GDL porosity, ε_{GDL}	0.5		Per design
Separator plate density	2210	$kg\,m^{-3}$	Per design
Separator plate specific heat	0.5	$kJ\,(kg\,K)^{-1}$	Per design
Electrolyte dry density	2200	$kg\,m^{-3}$	Per design
Electrolyte dry equivalent weight	1000	$kg\,kmol^{-1}$	Per design
Electrolyte solid specific heat	2.179	$kJ\,(kg\,K)^{-1}$	Per design
Separator plate conduction coefficient	0.22	$kW\,(m\,K)^{-1}$	Per design
Nusselt number of anode gas, *Nu*	2.96		[15]
Nusselt number of cathode gas	2.96		[15]
Nusselt number of coolant	7.54		[15]
Sherwood number for anode gas, *Sh*	12.5		[15]
Sherwood number for cathode gas	12.5		[15]
Diffusion coefficient for hydrogen	4.1E−5	$m\,s^{-1}$	[18]
Diffusion coefficient for oxygen	2.1E−5	$m\,s^{-1}$	[18]
Diffusion coefficient for nitrogen	2.2E−5	$m\,s^{-1}$	[18]
Diffusion coefficient for hydrogen	2.6E−5	$m\,s^{-1}$	[18]

to calculate temperatures, concentrations, and in this case, electrical energy consumption. The only inputs are current, ambient temperature, and water flow rate, temperature, and pressure to the anode. The model operates on current control and calculates electrolyzer voltage (including losses) and anode and cathode exit flow rates, temperatures, and species compositions. Unlike the fuel cell model, the electrolyzer does not include any separate provisions for cooling because the inlet water is used to cool the stack during all operating conditions. The pressurized inlet water is supplied at a constant $100\,g\,s^{-1}$, regardless of current, whenever the electrolyzer is operating. At maximum power consumption of 3.6 kW, the water consumed by electrolysis is just $0.182\,g\,s^{-1}$. The difference in water consumed versus flow rate provides sufficient cooling. Additionally, the electrolyzer model has no anode GDL because the entire anode side of the cell is flooded. These differences are shown in the electrolyzer model schematic of Fig. 4. It is assumed that the anode bulk flow and reaction sites are at the same temperature, and that as long as the water flow rate to the electrolyzer is sufficient, then

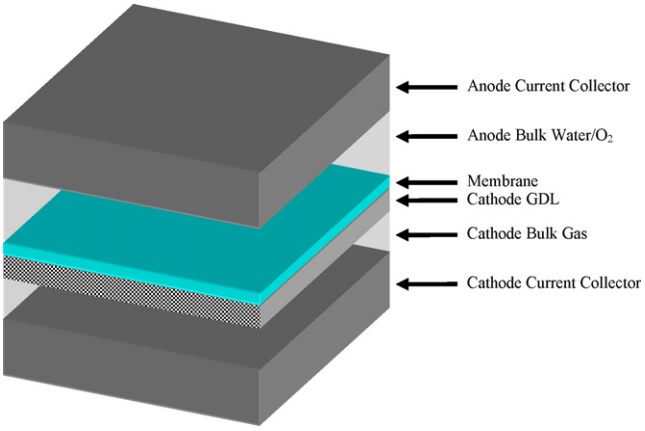

Fig. 4. Diagram showing six control volumes modeled for the electrolyzer.

Table 4
Electrolyzer model parameters

Parameter	Value	Units	Reference
Number of cells in series	15	NA	Per design
Exchange current density, i_0	0.01	$A\,m^{-2}$	[20]
Activation polarization coefficient, a_c	0.5		[20]
Operating pressure, P_o	6.8	atm	Per design
Dimension of cell	0.13×0.13	m	Per design
Air utilization, μ_{air}	50	%	Per design
Depth of anode gas channel	0.01	m	Per design
Depth of cathode gas channel	0.001	m	Per design
Thickness of GDL, t_{GDL}	0.0002	m	Per design
Thickness of electrolyte	0.00015	m	Per design
Thickness of separator plates	0.002	m	Per design
GDL porosity, ε_{GDL}	0.5		Per design
Separator plate density	2210	$kg\,m^{-3}$	Per design
Separator plate-specific heat	0.5	$kJ\,(kg\,K)^{-1}$	Per design
Electrolyte dry density	2200	$kg\,m^{-3}$	Per design
Electrolyte dry equivalent weight	1000	kg kmol	Per design
Electrolyte solid-specific heat	2.179	$kJ\,(kg\,K)^{-1}$	Per design
Separator plate conduction coefficient	0.22	$kW\,(m\,K)^{-1}$	Per design
Nusselt number of anode fluid, *Nu*	7.54		[15]
Nusselt number of cathode gas	2.96		[15]
Sherwood number for cathode gas	12.5		[15]
Diffusion coefficient for hydrogen	4.1E−5	$m\,s^{-1}$	[18]
Diffusion coefficient for oxygen	2.1E−5	$m\,s^{-1}$	[18]
Diffusion coefficient for hydrogen	2.6E−5	$m\,s^{-1}$	[18]

there is always liquid water at the anode catalyst sites with no diffusion limitations in this region. The MEA therefore consists of only a membrane and the cathode GDL. An additional difference between the fuel cell and electrolyzer models is that no nitrogen is included in any of the electrolyzer control volumes. Otherwise, the same set of equations as those used in the fuel cell model are simultaneously solved in each time step in the electrolyzer model.

2.3.1. Electrolyzer electrochemistry

As in the fuel cell component model, the rates of the electrochemical reactions in the electrolyzer are assumed instantaneous because the timescales of these reactions are far faster than those associated with the other physics in the model. The electrochemical potential of the electrolyzer is modeled using the Nernst equation coupled with equations for ohmic and activation polarization losses:

$$V = -\frac{\Delta G(T)}{nF} + \frac{RT}{nF}\ln\left[\frac{X_{H_2}X_{O_2}^{1/2}}{X_{H_2O}}P^{1/2}\right] + a_c\frac{RT}{nF}\ln\left(\frac{i}{i_0}\right) + iR \qquad (35)$$

The only differences between Eq. (31) for the fuel cell and Eq. (35) for the electrolyzer are sign changes on the activation and ohmic loss terms. The rates of all reactions are again proportional to the current:

$$\dot{n}_{react} = \frac{i}{nF} \qquad (36)$$

Concentration polarization has been neglected due to the fact that the electrolyzer never operates at high current density conditions. Ohmic resistance in the electrolyzer is a function of water content. The electrolyzer model ends up predicting ohmic losses that are relatively low because the anode is always flooded, reducing water content variation in the membrane. Like the fuel cell, both anode and cathode compartments are pressurized at the same level during operation. By pressurizing the anode inlet water, the use of a separate hydrogen compressor that would otherwise be needed to generate the pressure required by the hydride tank can be sidestepped.

2.3.2. Model parameters

Table 4 lists various parameters used in the electrolyzer model.

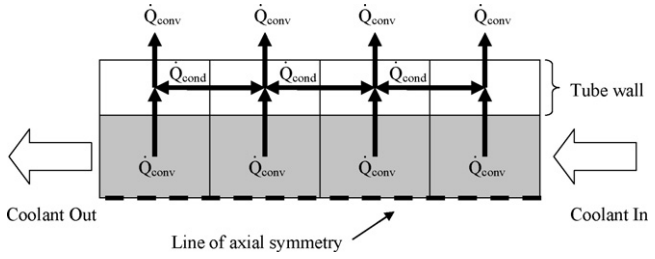

Fig. 5. Heat transfer pathways of radiator module.

2.4. Radiator

A first principles model of a simple, one dimensional, tube and fin radiator consisting of four adjacent nodes has been developed to simulate the system radiator. This radiator serves to cool the hydride tank during charging and to cool the fuel cell during power mode. Fig. 5 shows a diagram of the heat transfer modes in the tube of the radiator. Convection heat transfer occurs between the coolant and the inner tube wall, heat conduction occurs between the tube nodes, and convective heat transfer with the environment occurs on the outer tube wall. The gas exit temperatures of each node are used to calculate the temperature differences needed for the convection heat transfer equation (37) between the coolant and the tube wall. The equation for heat convection, $\dot{Q}_{convection}$, between coolant and tube at each node is calculated as

$$\dot{Q}_{convection} = h_{coolant} A_i (T_{coolant\_out} - T_{tube}) \quad (37)$$

where $h_{coolant}$ is the coolant convection heat transfer coefficient, A_i is the internal tube surface area, and $T_{coolant\_out}$ and T_{tube} are the exit coolant temperature and tube nodal temperature, respectively. Convection heat transfer between the tube and the environment is

$$\dot{Q}_{convection} = h_{environ} A_e (T_{tube} - T_{environ}) \quad (38)$$

where $h_{environ}$ is the ambient environmental convection heat transfer coefficient, A_e is the external tube surface area, and T_{tube} and $T_{environ}$ are the tube nodal temperature and ambient temperature, respectively. Conduction along the length of the tube is calculated similarly to Eq. (9). Table 5 lists the parameter values used in the radiator model.

2.5. Ancillary components

Several other important components have been modeled empirically to complete the system. A simple on–off 100 W radiator fan provides the forced convection necessary to remove heat from the radiator. When the fan is off, the radiator is cooled by natural convection with the ambient environment. When the fan is turned on, the convection heat transfer coefficient between the radiator tube and the environment is increased to simulate forced convection. Another ancillary component is a constant power 200 W coolant pump that circulates the coolant fluid at a continuous 0.33 kg s^{-1} during all modes of system operation. The final ancillary component modeled is a variable speed fuel cell inlet air blower. The blower power is proportional to the cube of the required air flow [21] with a maximum power level of 540 W at an air flow rate of 0.218 mol s^{-1}. The required air flow rate at any fuel cell operating point is determined from the fuel cell current level and the desired oxidant utilization factor, μ_{air}:

$$\dot{n}_{air} = \frac{i}{4F\mu_{air}\chi_{O_2}} \quad (39)$$

X_{O_2} is the oxygen mole fraction in air and the 4 is due to 4 mol of electrons transferred per mole of oxygen gas.

Table 5
Radiator model parameters

Parameter	Value	Units
Tube conduction coefficient, k	237	W (m K)$^{-1}$
Coolant to tube convection coefficient, h_{ct}	500	W (m^2 K)$^{-1}$
Air to tube convection coefficient, h_{at}	50 if fan is on; 0.5 if fan is off	W (m^2 K)$^{-1}$
Tube length, l_t	2.54	m
Tube thickness, t_t	0.001	m
Tube inner diameter	0.024	m
Tube density	2700	kg m^{-3}
Tube specific heat	903	J (kg K)$^{-1}$
Coolant density	1000	kg m^{-3}
Coolant-specific heat	4200	J (kg K)$^{-1}$
Coolant flow rate	0.33	kg s^{-1}

3. System interfaces

Fig. 6 shows a diagram of the physical interfaces between RFC components in the current model. During charging mode, the electrolyzer is supplied with electrical current and deionized water while the hydrogen produced is absorbed exothermically by the hydride tank. The heat from this reaction is removed by a circulating water bath cooled by the radiator. In power mode, the electrolyzer is turned off and the fuel cell produces power from hydrogen supplied by the endothermic desorption of hydrogen from the metal hydride bed. Simultaneously, the heat generated by the fuel cell is removed via liquid cooling and fed to the hydride tank water bath to simultaneously provide the necessary energy for hydrogen evolution and be cooled by this endothermic process. The exiting water is then further cooled by the radiator before re-entering the fuel cell.

The three numbered boxes in Fig. 6 represent model processes in which the dynamics of the extant physics are not accounted for. Box number 1 represents an enthalpy exchange device (e.g., enthalpy wheel) that is simplified to set the temperature and humidity of the incoming air to 65 °C and 30% relative humidity, respectively, regardless of the ambient conditions. Box number 2 simulates a throttling and enthalpy exchange process wherein hydrogen pressure drops from the internal hydride tank pressure down to the fuel cell inlet pressure (110 kPa), and the temperature and humidity are increased to 65 °C and 75% relative humidity, respectively, via an assumed enthalpy exchange with the fuel cell cathode exhaust. The total enthalpy of the stream exiting box number 2 is equal to the total enthalpy of the stream entering box number 2. The internal hydride tank pressure is governed by the tank temperature (Eq. (2)) and is always controlled to be greater than, or equal to the fuel cell inlet pressure, as explained in the following controls section. The maximum tank pressure is controlled to be 689.5 kPa. Therefore, the largest possible pressure drop during the throttling expansion would be 579.5 kPa. Using a Joule–Thomson coefficient for room temperature hydrogen of 4.0E−4 K kPa^{-1} [22], the temperature change during the expansion due to the Joule–Thomson effect can be shown to be negligible, which supports the current simplification of this process as follows [23]:

$$\mu_J = \left(\frac{\partial T}{\partial P}\right)_h \quad (40)$$

$$\Delta T = \mu_J \Delta P = 4 \times 10^{-4}\,\mathrm{K\,kPa^{-1}} \times 579.5\,\mathrm{kPa} = 0.23\,\mathrm{K} \quad (41)$$

Box number 3 simulates a similar reduction in pressure and a reduction of humidity process wherein the outlet electrolyzer pressure (689 kPa) is reduced to the necessary tank inlet pressure, and

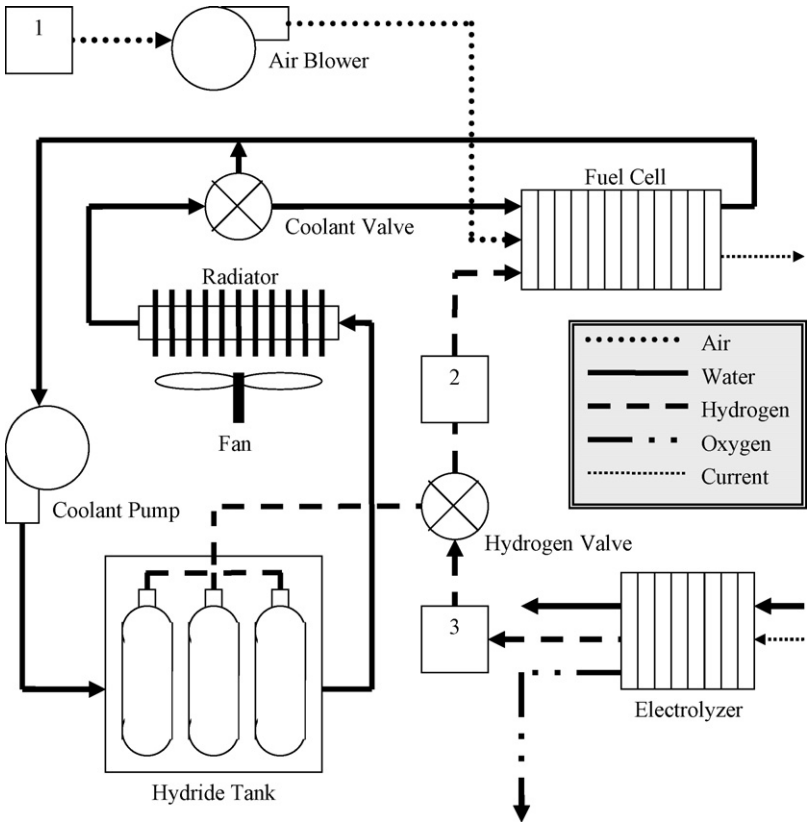

Fig. 6. Diagram of RFC system model. Numbered boxes represent state changes in which the physics are not fully modeled.

the gas is dried to 0% relative humidity (e.g., by using a desiccant). Again, the electrolyzer pressure is controlled to always be greater than, or equal to the tank inlet pressure.

4. Results

4.1. System control

Several interesting situations can arise during operation of this system. During the initial stages of system charging, the electrolyzer maximum hydrogen production rate will be the bottleneck because the hydride tank is cool, empty, and can accept a larger flow of hydrogen than the electrolyzer can produce. However, as the hydride tank fills and heats during charging, the available fill rate slows, eventually reaching the point where the rate at which the tank can fill drops below the rate at which the electrolyzer can produce hydrogen. The model accounts for this by calculating a line pressure between the electrolyzer and the hydride tank using the Ideal Gas Law:

$$P = \frac{nRT}{V} \tag{42}$$

where the number of moles, n, in the line volume can be found by integrating a molar balance:

$$\frac{dn}{dt} = \dot{n}_{elec} - \dot{n}_{tank} \tag{43}$$

Here $\dot{n}_{elec}$ is the molar flow rate of hydrogen produced by the electrolyzer and $\dot{n}_{tank}$ is the molar flow rate of hydrogen entering the hydride tank. The electrolyzer always produces hydrogen output at 689 kPa because the water supplied to the electrolyzer is pressurized to 689 kPa. Initially, the line pressure stays well below 689 kPa because the rate of hydrogen absorbed by the tank is nearly identical to the rate produced by the electrolyzer, and little mass can accumulate in the line between the two components. During this operating condition, the tank fills at a linear rate proportional to the electrolyzer's maximum output. As the tank fill rate slows due to tank heating and fill level (Eqs. (1) and (2)), the line pressure builds, eventually reaching 689 kPa. As this threshold is approached, a proportional and triggered integral controller based on pressure feedback reduces the current powering the electrolyzer in order to maintain the maximum line pressure. The system transient response to this charging situation is shown in Fig. 7. Note that electrolyzer current is reduced considerably once the pressure reaches 7 bar, but, that the hydride tank continues to fill (albeit at a slower rate).

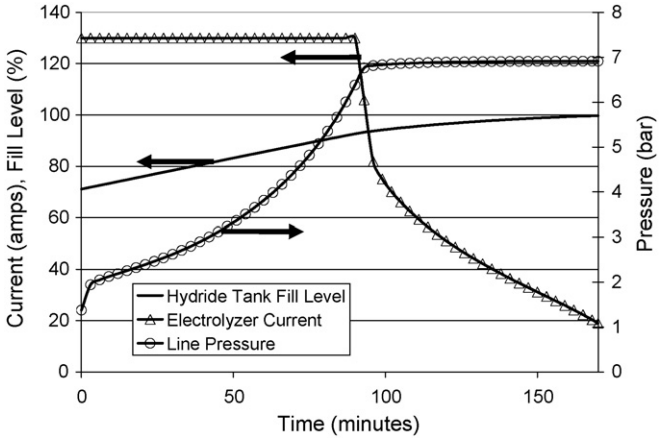

Fig. 7. RFC transient response during charging operation with increasing tank fill level.

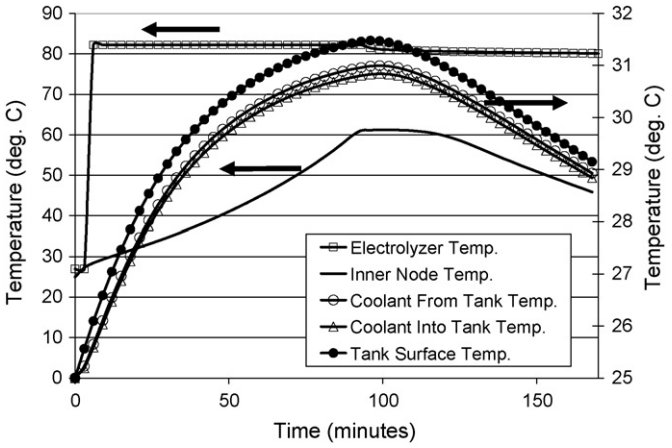

Fig. 8. RFC temperature responses during charging operation with increasing tank fill level.

Fig. 8 shows temperature information during the same filling event. The temperature profiles for the electrolyzer membrane and inner node of the hydride tank are plotted on the left axis and the temperature profiles for the surface of the hydride tank and the coolant water into and out of the hydride cooling chamber are plotted on the right, to better distinguish the relatively small temperature differences between them. It can be seen that the electrolyzer reaches an operating temperature of roughly 80 °C within several minutes, and maintains this temperature throughout the fill event. The inner node of the hydride tank warms fairly steadily until this portion of the tank becomes saturated (around 100 min) at which time the temperature steadily decreases because the exothermic reaction has stopped. Despite the inner tank temperature rising by almost 40 °C, the tank surface temperature only rises 6.5 °C due to contact with the coolant bath and the poor heat transfer properties of the powdered metal hydride material. The coolant temperatures show that relatively little energy is transferred from the tank to the coolant (because of the small temperature difference between the coolant inlet and outlet temperature), underscoring the rate-determining effect of hydride tank heat transfer.

Fig. 9 shows a diagram of the strategy for controlling electrolyzer current. This controller is designed to complete the charging process as quickly as possible by first operating at the maximum electrolyzer output, and then transitioning to operate at the maximum allowable system/line pressure as the hydride tank filling rate becomes the system bottleneck. This charging strategy is logical for an onboard military applications where alternator power is plentiful and maximum charge rate is more important than overall system efficiency. However, one can easily imagine different charging priorities (e.g., to maximize efficiency or minimize cost by reducing component sizes) not considered here.

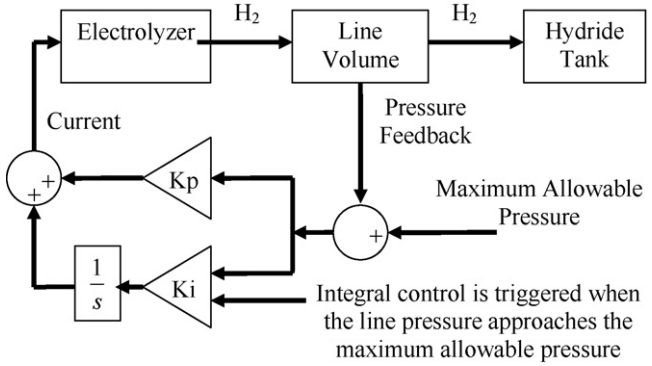

Fig. 9. Diagram of electrolyzer current control strategy.

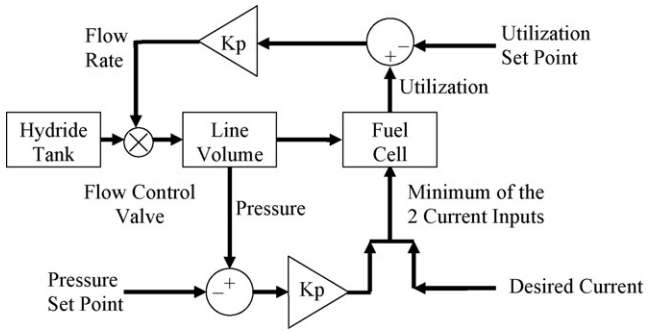

Fig. 10. Diagram of fuel cell current and gas flow rate control strategy.

Another intriguing situation can occur during fuel cell operation if the power requested from the fuel cell is greater than that available from the tank. An approach similar to that of the electrolyzer is taken whereby the gas pressure in a line volume between the tank outlet and fuel cell inlet is simulated based on the Ideal Gas Law and a dynamic molar balance equation. The fuel cell inlet pressure is 110 kPa requiring that the line pressure not drop below this value. Additionally, fuel utilization is controlled to maintain cell voltage and ensure efficient operation.

The fuel cell control strategy uses pressure feedback to control current. If the line pressure is greater than the minimum pressure, the current will default to the desired current. If the tank cannot supply enough fuel, the line pressure will drop, and the current will be reduced proportionally to match the hydrogen supply available.

The secondary utilization control loop uses a utilization error signal to proportionally control the fuel flow rate. This double controller configuration enables current and utilization to be controlled even as the hydrogen supply is diminished. Fig. 10 shows a diagram illustrating both fuel cell controllers.

Fig. 11 shows the system response during low fuel level operation. The current is stable at the desired level of 100 A until the line pressure drops to 110 kPa, at which point the current and hydrogen flow rate drop to ensure sufficient pressure and to maintain 80% fuel utilization. The plot demonstrates how excess hydrogen pressure is initially available as the fuel cell waste heat aides the hydride desorption reaction. The hydride tank empties at a nearly linear rate as the system operates at constant power. However, when the tank fill level falls, the desorption reaction slows and the pressure available

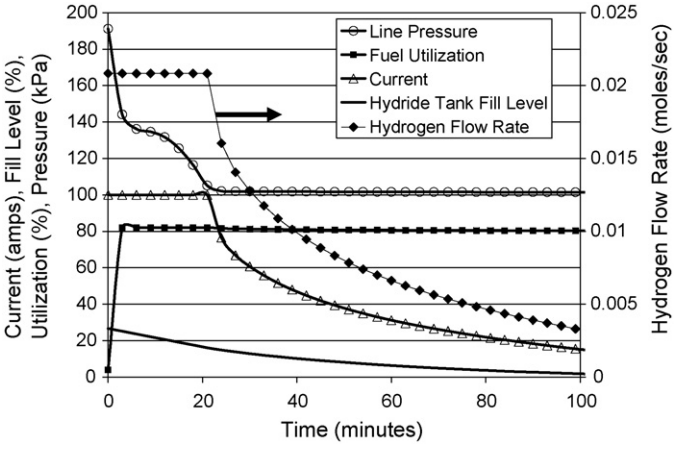

Fig. 11. RFC transient response during power operation with diminishing fuel level in the hydride tank.

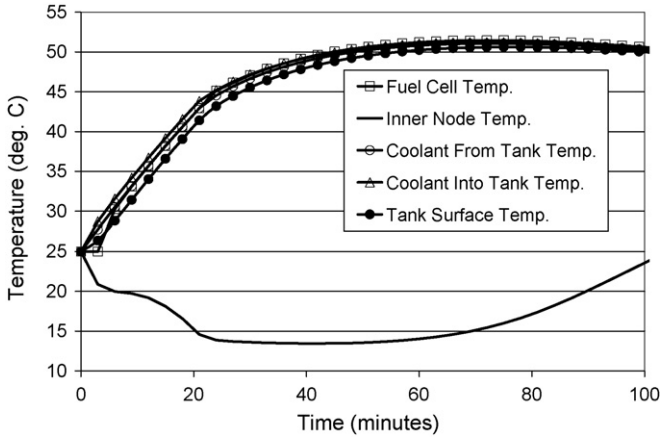

Fig. 12. RFC temperature responses during power operation with diminishing fuel level.

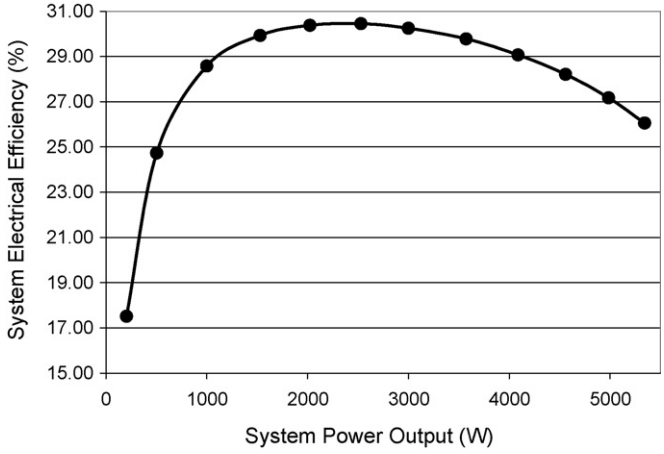

Fig. 13. System round-trip efficiency as it varies with system power output.

from the tank drops. Note that a nearly constant fuel utilization of 80% is maintained throughout the operation. The inconsistent line pressure decrease during the first 20 min of operation can be accounted for by a drastic initial pressure decrease as the fuel cell begins using fuel, then a leveling off portion as the waste heat from the fuel cell begins to aid hydrogen flow from the tank, then a second, less severe pressure reduction caused by decreased hydrogen supply as the tank level drops.

Fig. 12 shows temperature results for the fuel cell power event. The temperatures of the fuel cell membrane, hydride tank surface, coolant into the tank, and coolant out of the tank all follow the same profile. They rise steadily for the first 20 min, then begin to level off and even slightly decrease after the fuel cell current is reduced by the controller. The internal temperature of the hydride tank falls below room temperature as the endothermic hydrogen desorption reaction occurs, but cannot fully utilize the fuel cell waste heat due, again, to the poor heat transfer characteristics of the tank. The radiator plays no roll in this scenario because the fuel cell never reaches its design set point temperature of 80 °C.

4.2. System efficiencies

The RFC system presented herein is relatively simple and self-contained. Apart from the electrolyzer, the only energy consuming devices are a variable power 0–540 W blower for fuel cell inlet air, a 100 W radiator fan, and a 200 W water pump. System efficiency for any operating period can therefore be defined by Eq. (44):

$$\eta_{\text{electrical}} = \frac{E_{\text{fuel cell}} - E_{\text{blower}} - E_{\text{FC\_pump}} - E_{\text{FC\_fan}}}{E_{\text{electrolyzer}} + E_{\text{E\_pump}} + E_{\text{E\_fan}}} \quad (44)$$

where $E_{\text{fuel cell}}$ and $E_{\text{electrolyzer}}$ are the quantities of electrical energy supplied by the fuel cell and delivered to the electrolyzer, respectively. The electrical energy required for the blower, E_{blower}, is accounted for as well as the energy used by the fan and pump during electrolysis, $E_{\text{E\_fan}}$, $E_{\text{E\_pump}}$, and during fuel cell operation, $E_{\text{FC\_fan}}$, $E_{\text{FC\_pump}}$.

System round-trip efficiencies have been tabulated for various system power levels as shown in Fig. 13. Due to the diminishing hydrogen desorption rate as the level in the hydride tank falls, no power set point can be maintained for an entire tank of fuel. For example, a system power output of 3.0 kW can be maintained as the tank drains from 100% fill level to 50%, or a system power of just 50 W can be maintained all the way down to a tank level of 5.5%, but once each of these respective levels is reached, the hydrogen flow rate becomes so small that the fuel cell current controller must reduce the current output to maintain the necessary fuel line pressure. To compare system efficiencies at different power levels on the same basis, the efficiencies shown in Fig. 13 are calculated by operating at constant power from a 100% full tank only until that particular power level can no longer be maintained, and then switching to charge mode to fill the tank back to 100%. This means that the total energy (power multiplied by time) stored and delivered for each point on the efficiency curve is not necessarily the same.

The lower efficiencies observed at low power levels are due to relatively high parasitic loads, such as the constant 200 W cooling pump load. The decrease in efficiency at high power levels is due to reduced fuel cell and electrolyzer efficiency at higher loads combined with increased parasitic losses from the variable power fuel cell air inlet blower. It is important to note that the cooling system fan never operated during any of the power cycles presented in Fig. 13 because the fuel cell never reached the design operating temperature of 80 °C. Though the internal fuel cell temperature gradually increased throughout operation at each power level (in a similar fashion to that shown in Fig. 12), the endothermic hydrogen desorption reaction in the hydride tank removed sufficient heat from the coolant stream to keep the fuel cell temperature below its high temperature limit. A larger hydrogen storage tank may have allowed the simulated operation to continue long enough for the fuel cell to eventually reach the maximum operating temperature. This cooling phenomenon can help explain the fairly flat mid-range efficiency shown in Fig. 13. In the current PEM fuel cell model, efficiency decreases as power level increases and fuel cell efficiency increases with increasing temperature. Therefore, since the fuel cell temperature never reaches an upper boundary during the simulations, the efficiency losses due to higher current density operation are offset by the efficiency gains reached through the gradually higher temperature operation.

Figs. 14 and 15 show the power outputs and inputs for each of the system components during transient operation of a charge/discharge cycle from an initial hydride tank level of 25–95% and back to 25% at a constant current set point. Both plots are identical during the tank filling portion of the operation because the electrolyzer fills the tank from 25 to 95% at the maximum rate as described previously. In Fig. 14 (Case 1), after reaching a tank level of 95%, the electrolyzer is turned off and the fuel cell is operated at approximately 1.35 kW (50 A) until the tank has been drained back to a 25% level. After subtracting parasitic pump and fan loads, this equates to a system output power of roughly 1.15 kW. Fig. 14 shows that the system is capable of maintaining this power output level for the duration of the test (275 min).

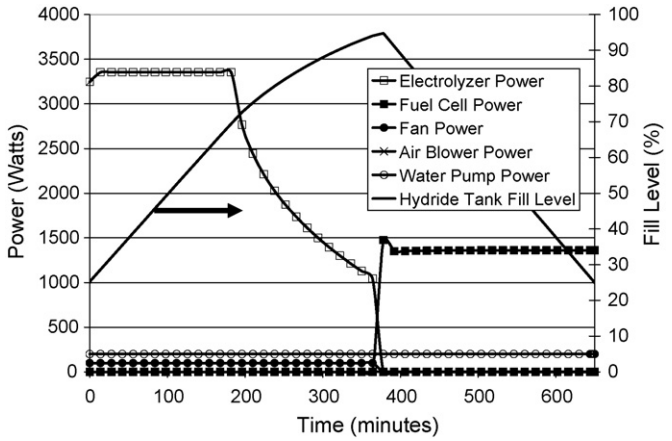

Fig. 14. Transient RFC system response (Case 1) showing component power levels beginning with charging mode and switching to power mode after 377 min. The system then maintains a constant power output of roughly 1.15 kW until the completion of the simulation.

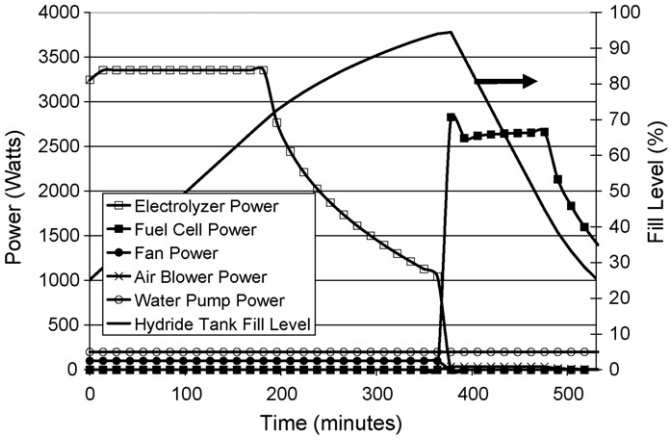

Fig. 15. Transient RFC system response (Case 2) showing component power levels beginning with charging mode and switching to power mode after 377 min. The system then attempts to maintain a constant power output of 2.4 kW.

Fig. 15 shows Case 2 which has a similar charge and discharge cycle but with a larger fuel cell power output of approximately 2.70 kW (100 A) corresponding to a system power of approximately 2.4 kW. It can be seen that the system is unable to maintain this higher power level for the duration of the test. Fig. 15 shows a moderate output power improvement as the fuel cell performance increases due to the steady temperature rise of the stack, but after 107 min, the current controller begins to reduce fuel cell power as hydrogen flow becomes limited. At this point, the fuel cell waste heat carried by the cooling fluid to the hydride tank is insufficient to remove the quantity of gas required by the fuel cell. This occurs because the hydrogen flow rate from the tank slows as the tank level drops. It should also be noted that the radiator cooling fan was not powered because the coolant temperature never reached the "fan on" threshold.

Table 6 lists this energy data and the corresponding overall system efficiencies for both simulation cases.

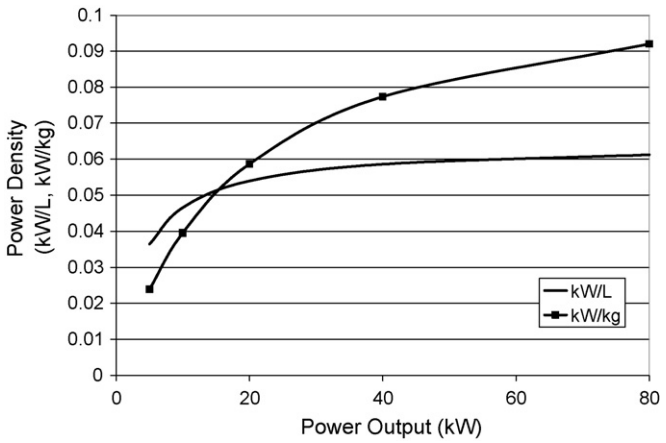

Fig. 16. Maximum theoretical volumetric and gravimetric power densities for an RFC system utilizing components that possess performance characteristics similar to those commercially available.

The efficiency of 29.8% calculated in Table 6 for operation at 1.15 kW is slightly higher than the efficiency predicted by Fig. 13 for the same power output (29.1%). This is because the charge portion of the cycle evaluated in Fig. 13 fills the tank all the way to 100%, instead of just 95%. This small difference in fill level has a significant effect on overall efficiency because of the constant parasitic load of the 200 W water pump. Although the electrolyzer is operating very efficiently during the final 5% of the fill because the hydride tank absorption rate at this point is so slow (low current density operation of the electrolyzer), the water pump continues to work at full power, lowering the system efficiency. A similar effect occurs with Case 2 for operation at 2.40 kW. These types of insights, often not included in systems analyses that only simulate the major components, are important to understand for the design and operation of complete RFC systems.

4.3. Energy and power density

The RFC system studied in this analysis could be built by using currently available commercial products. A 4 kW Hydrogenics HyLYZER PEM electrolyzer and a 5 kW Hydrogenics HyPM fuel cell [24] could be used in conjunction with 10,000 standard liters of hydrogen storage in the form of three metal hydride tanks available from GfE Metalle und Materialien, GmbH of Nürnberg, Germany. The dimensions of each component, as well as those for the standard military lead-acid battery ("6TMF") currently used in the Stryker vehicle [25], and a commercially available lead-acid battery ("Hawker Genesis G70EP") [26] are given in Table 7. The Hawker Genesis is included because of the wealth of performance data available from the manufacturer and in the literature. Numbers in the gray regions are actual values provided by manufacturers. Values listed in the non-shaded areas are estimates used in the current model.

The gravimetric and volumetric energy densities given in Table 7 clearly indicate that the hypothetical RFC system analyzed herein is not currently competitive with lead-acid battery technology on a pure energy density basis. Likewise, an RFC system cannot produce nearly as much power on a mass or volume basis as a lead-acid bat-

Table 6
Energies and overall system efficiencies for the two RFC operation cases

Operating condition	$E_{electrolyzer}$ (MJ)	E_{E_pump} (MJ)	E_{E_fan} (MJ)	$E_{fuel\ cell}$ (MJ)	E_{blower} (MJ)	E_{FC_pump} (MJ)	E_{FC_fan} (MJ)	$\eta_{electrical}$ (%)
Case 1	57.25	4.536	2.268	22.430	0.071	3.276	0.0	29.8
Case 2	57.25	4.536	2.268	21.893	0.2507	1.848	0.0	30.9

Table 7
RFC system component and lead-acid battery dimensions, and calculated energy and power densities

Component	Volume (Liter)	Mass (kg)	Energy Output (MJ)	Power Output (kW)	Volumetric Energy Density (kJ L^{-1})	Gravimetric Energy Density (kJ kg^{-1})	Power /Vol (kW L^{-1})	Power /Mass (kW kg^{-1})
Lead acid battery, 6TMF	15	33.5	5.18[a]	NA	346	156	NA	NA
Lead acid battery, G70EP	9.8	24.3	3.38[a]	3.68[b]	345	139	0.38	0.14
Hydrogenics HyPM10[c]	78	44.0						
Hydrogenics HyLYSER 2.0	34	30.0						
10,000 liter hydride tank	20	125						
Tank cooling bath and enclosure	25	10.0						
System total	137	209	18.9[d]	5.0	138	90	0.036	0.024

[a]Energy output during C20 discharge cycle. [b]Power output sustainable for 5 min. [c]Product specifications were available only for a 10 kW fuel cell, not a 5 kW cell as studied in this analysis. Therefore, the size and weight of the 10 kW fuel cell were halved to estimate the specifications for the smaller cell. [d]System energy output during continuous 1.15 kW operation.

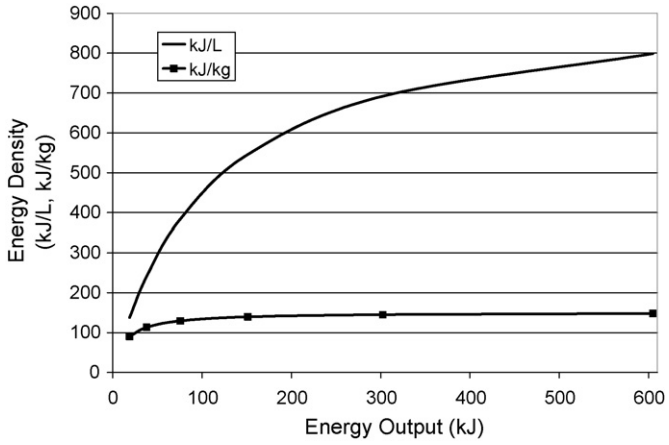

Fig. 17. Maximum theoretical volumetric and gravimetric energy densities for an RFC system utilizing components that possess performance characteristics similar to those commercially available.

tery. However, the storage capability of the RFC is close enough to that of the battery that one can envision niche applications where the theoretically superior cyclic durability, modular design, and lack of self-discharge properties of the RFC system may outweigh the energy density deficiency as compared to traditional battery technology. The scope of such niche applications will only increase as RFC components and systems are optimized. In addition, improvements in the energy and power density of RFC system components are expected in the future, which could significantly improve competitiveness with battery systems.

Because of the disassociated nature of the power and energy performance characteristics of an RFC system, it is easy to project the theoretical maximum energy and power densities attainable with given component technology performance. The energy density can clearly never exceed the basic energy density of the particular hydrogen storage tank used. Likewise, the power output can never exceed the power output of the fuel cell. A limiting case for both scenarios is reached as the tank or fuel cell size is increased to the point where the sizes of the other components become insignificant, as shown in Figs. 16 and 17. These projections assume that the power output and hydrogen stored increase linearly with size and mass of the fuel cell and tank, respectively. Though fuel cell power does increase linearly with electrode surface area, and hydrogen storage does increase linearly with the mass of metal hydride, an actual larger system may offer greater performance gains than predicted here due to the non-linear performance-to-size changes of balance of plant equipment components, such as blowers and pumps. These projections can therefore be considered a "worst case" scenario. Figs. 16 and 17 show maximum power densities approaching 0.1 kW kg^{-1} and 0.06 kW L^{-1} and maximum energy densities of more than 800 kJ L^{-1} and 150 kJ kg^{-1}, respectively. This shows that the potential volumetric energy density of an RFC system far exceeds that of a lead-acid battery while the potential gravimetric energy density is roughly equivalent, with current metal hydride, PEM fuel cell and PEM electrolyzer performance characteristics.

5. Summary and conclusions

An RFC system model has been built using first principles approaches for all of the major system components and simple feedback control strategies for the system interfaces. The model has been exercised and shown to demonstrate reasonable system transient responses during all modes of operation. The following conclusions can be drawn from simulations conducted with this model:

- Charge rate is at first governed by electrolyzer power. The hydride tank fill rate will then slow to a point where it becomes the rate limiting factor. The fill rate of the first portion of the charging bottleneck can be increased by installing a larger electrolyzer. The charging rate in the second regime can be increased by enabling better cooling of the hydride tank. The transition point is determined by the electrolyzer and hydride tank sizes.
- System power output during power mode is governed at first by fuel cell size and later by hydrogen flow rate. The maximum power output can be raised by increasing the capacity of the fuel cell, whereas system runtime at a particular power level can be increased by using a larger hydride tank.
- If integrated cooling loops are used, metal hydride material should be carefully chosen for a particular application, not only in order to efficiently store hydrogen, but also to allow fuel cell operation at the design temperature to enable operation at maximum efficiency.
- While major component efficiencies may improve for various operating conditions during dynamic operation, it is important to capture the interactions with other system components and balance of plant items to determine overall system performance.
- Variable power balance of plant components can greatly reduce parasitic losses for a system with a wide dynamic operating power range. Of course, variable power components can increase system cost and control complexity.

References

[1] W. Smith, J. Power Sources 86 (2000) 74–83.
[2] A. Bergen, et al., J. Power Sources 164 (2007) 624–630.
[3] K. Bolwin, J. Power Sources 40 (1992) 307–321.
[4] F. Barbir, T. Molter, L. Dalton, Int. J. Hydrogen Energy 30 (2004) 351–357.
[5] Defense Board Science Task Force on Improving Fuel Efficiency of Weapons Platforms, "More Capable Warfighting Through Reduced Fuel Burden," Report to the Office of the Under Secretary of Defense for Acquisition, Technology, and Logistics, Washington, DC, January 2001.
[6] G. Sandrock, State-of-the-Art—Review of Hydrogen Storage in Reversible Metal Hydrides for Military Fuel Cell Applications, Department of the Navy, Office of Naval Research, 1997.
[7] O. Ulleberg, Int. J. Hydrogen Energy 28 (2003) 21–33.
[8] S. Busquet, C.E. Hubert, J. Labbé, D. Mayer, R. Metkemeijer, J. Power Sources 134 (2004) 41–48.
[9] M.J. Khan, M.T. Iqbal, Renew. Energy 30 (2005) 421–439.
[10] H. Görgün, Int. J. Hydrogen Energy 31 (2006) 29–38.
[11] J. Maclay, J. Brouwer, G.S. Samuelsen, Int. J. Hydrogen Energy 31 (2006) 994–1009.
[12] T. Brown, J. Brouwer, G.S. Samuelsen, Int. J. Hydrogen Energy, in revision, April 2008.
[13] U. Mayer, M. Groll, W. Supper, J. Less-Common Met. 131 (1987) 235–244.
[14] A. Jemni, S. Nasrallah, J. Lamloumi, Int. J. Hydrogen Energy 24 (1999) 631–644.
[15] F. Incropera, D. DeWitt, Fundamentals of Heat and Mass Transfer, John Wiley and Sons, 1996.
[16] S. Gadre, et al., Ind. Eng. Chem. Res. 42 (2003) 1713–1722.
[17] S. Suda, N. Kobayashi, J. Less-Common Met. 73 (1980) 119–126.
[18] F. Mueller, J. Brouwer, S. Kang, H. Kim, K. Min, J. Power Sources 163 (2007) 814–829.
[19] T.E. Springer, T.A. Zawodzinski, S. Gottesfeld, J. Electrochem. Soc. 138 (1991) 2334–2342.
[20] J. Larminie, A. Dicks, Fuel Cell Systems Explained, second ed., Wiley, 2003.
[21] R. Fox, A. McDonald, Introduction to Fluid Mechanics, fourth ed., Wiley, New York, 1992.
[22] E. Herrck, L. Johnston, I. Bezman, C. Hood, J. Am. Chem. Soc. 68 (1946) 2367–2373.
[23] M. Moran, H. Shapiro, Fundamentals of Engineering Thermodynamics, John Wiley & Sons, 1995.
[24] http://www.hydrogenics.com.
[25] http://www.milbatteries.com/hawker/brochure.html.
[26] EnerSys Genesis Selection Guide, fifth ed., US-GPL-SG-002, July 2006.